

THE ERA OF STAR FORMATION IN GALAXY CLUSTERS

M. BRODWIN¹, S. A. STANFORD², ANTHONY H. GONZALEZ³, G. R. ZEIMANN⁴, G. F. SNYDER⁵, C. L. MANCONE³, A. POPE⁶, P. R. EISENHARDT⁷, D. STERN⁷, S. ALBERTS⁶, M. L. N. ASHBY⁵, M. J. I. BROWN⁸, R.-R. CHARY⁹, ARJUN DEY¹⁰, A. GALAMETZ¹¹, D. P. GETTINGS³, B. T. JANNUZI¹², E. D. MILLER¹³, J. MOUSTAKAS¹⁴, AND L. A. MOUSTAKAS⁷

¹ Department of Physics and Astronomy, University of Missouri, 5110 Rockhill Road, Kansas City, MO 64110, USA

² University of California, Davis, CA 95616, USA

³ Department of Astronomy, University of Florida, Gainesville, FL 32611, USA

⁴ Department of Astronomy and Astrophysics, Pennsylvania State University, 525 Davey Laboratory, University Park, PA 16802, USA

⁵ Harvard-Smithsonian Center for Astrophysics, 60 Garden Street, Cambridge, MA 02138, USA

⁶ Department of Astronomy, University of Massachusetts, Amherst, MA 01003, USA

⁷ Jet Propulsion Laboratory, California Institute of Technology, Pasadena, CA 91109, USA

⁸ School of Physics, Monash University, Clayton, Victoria 3800, Australia

⁹ Spitzer Science Center, MC 220-6, California Institute of Technology, 1200 East California Boulevard, Pasadena, CA 91125, USA

¹⁰ National Optical Astronomy Observatory, 950 N. Cherry Avenue, Tucson, AZ 85719, USA

¹¹ INAF—Osservatorio di Roma, Via Frascati 33, I-00040 Monteporzio, Italy

¹² Steward Observatory, University of Arizona, 933 N. Cherry Avenue, Tucson, AZ 85121, USA

¹³ Kavli Institute for Astrophysics and Space Research, Massachusetts Institute of Technology, Cambridge, MA 02139, USA

¹⁴ Department of Physics and Astronomy, Siena College, 515 Loudon Road, Loudonville, NY 12211, USA

Received 2013 August 12; accepted 2013 October 19; published 2013 December 3

ABSTRACT

We analyze the star formation properties of 16 infrared-selected, spectroscopically confirmed galaxy clusters at $1 < z < 1.5$ from the *Spitzer*/IRAC Shallow Cluster Survey (ISCS). We present new spectroscopic confirmation for six of these high-redshift clusters, five of which are at $z > 1.35$. Using infrared luminosities measured with deep *Spitzer*/Multiband Imaging Photometer for *Spitzer* observations at $24 \mu\text{m}$, along with robust optical + IRAC photometric redshifts and spectral-energy-distribution-fitted stellar masses, we present the dust-obscured star-forming fractions, star formation rates, and specific star formation rates in these clusters as functions of redshift and projected clustercentric radius. We find that $z \sim 1.4$ represents a transition redshift for the ISCS sample, with clear evidence of an unquenched era of cluster star formation at earlier times. Beyond this redshift, the fraction of star-forming cluster members increases monotonically toward the cluster centers. Indeed, the specific star formation rate in the *cores* of these distant clusters is consistent with field values at similar redshifts, indicating that at $z > 1.4$ environment-dependent quenching had not yet been established in ISCS clusters. By combining these observations with complementary studies showing a rapid increase in the active galactic nucleus (AGN) fraction, a stochastic star formation history, and a major merging episode at the same epoch in this cluster sample, we suggest that the starburst activity is likely merger-driven and that the subsequent quenching is due to feedback from merger-fueled AGNs. The totality of the evidence suggests we are witnessing the final quenching period that brings an end to the era of star formation in galaxy clusters and initiates the era of passive evolution.

Key words: galaxies: clusters: general – galaxies: distances and redshifts – galaxies: evolution – galaxies: formation – galaxies: starburst

Online-only material: color figures

1. INTRODUCTION

Galaxies in the centers of nearby rich clusters and groups are passive, with little or no ongoing star formation. Most optical and near-IR (NIR) studies of the color and luminosity function evolution in cluster galaxies are consistent with a model in which cluster galaxies formed in short, vigorous bursts of star formation at high redshift ($z \gtrsim 2$) and evolved passively thereafter (e.g., Stanford et al. 1998; Blakeslee et al. 2006; van Dokkum & van der Marel 2007; Eisenhardt et al. 2008, hereafter E08; Mei et al. 2009; Mancone et al. 2010).

In contrast, recent mid-infrared (mid-IR) studies (e.g., Bai et al. 2009; Chung et al. 2010) have demonstrated that galaxies with high star formation rates (SFRs), including luminous and ultraluminous infrared galaxies (LIRGs and ULIRGs, defined as having $8-1000 \mu\text{m}$ IR luminosities, L_{IR} , of $10^{11} L_{\odot} \leq L_{\text{IR}} < 10^{12} L_{\odot}$ and $L_{\text{IR}} \geq 10^{12} L_{\odot}$, respectively), typically reside in the outskirts of present-day massive clusters. This suggests both an ongoing level of infall of gas-rich galaxies and groups

and a mechanism to quench the prodigious star formation of such recently accreted cluster members. Strangulation (Larson et al. 1980)—the stripping of galaxies’ hot gas reservoirs via interaction with the intracluster medium (ICM)—is the long-timescale (\sim few Gyr) mechanism typically invoked to explain the lack of subsequent star formation as a recently accreted galaxy is starved of fuel. At low redshift ($z < 0.1$), this environmental quenching is so effective that the fraction of star-forming galaxies in clusters is still below that in the field even at $3 r_{200}$ (Chung et al. 2011), where r_{200} ($\approx r_{\text{virial}}$) is the radius of the cluster within which the density is 200 times the critical density of the Universe.

Evolutionary studies have found a rapid growth in the frequency and intensity of the SFR in clusters. Saintonge et al. (2008) reported an increase in the fraction of rapidly star-forming cluster galaxies up to $z \sim 0.8$. The cluster mass-normalized integrated SFR was found to increase as roughly $(1+z)^5$ out to $z \sim 1$ (Bai et al. 2007, 2009; Krick et al. 2009), at least as rapidly as the field, albeit from a lower base. Several

other authors have found corroborating evidence of increased star formation activity in distant clusters out to $z \sim 0.8$, including a rising incidence of LIRGs and ULIRGs (e.g., Coia et al. 2005; Geach et al. 2006; Marcillac et al. 2007; Muzzin et al. 2008; Koyama et al. 2008; Haines et al. 2009; Tran et al. 2009; Smith et al. 2010; Webb et al. 2013). However, in all of these $z < 1$ studies cluster cores ($r \lesssim 0.25 r_{200}$) still show evidence of substantial quenching, with much lower central SFRs than are seen in the field.

Studies in deep field surveys have also addressed the effect of local density on star formation activity. Elbaz et al. (2007) and Cooper et al. (2008) found evidence that the relation between SFR and local galaxy density reverses at $z \sim 1$, in the sense that the SFR begins to increase with increasing density. Recent studies have reported LIRG-level IR luminosities in cluster galaxies at $z = 1.46$ (Hilton et al. 2010) and $z = 1.62$ (Tran et al. 2010). However, as Geach et al. (2006) demonstrate, there is a significant variation amongst clusters, even at moderate redshifts ($z \sim 0.5$).

The next step is to characterize the star formation properties of a large, uniformly selected sample of galaxy clusters at redshifts well beyond unity in order to study the epoch of cluster formation. In this paper, we study the SFR and specific SFRs (sSFRs) in 16 IR-selected, spectroscopically confirmed $1 < z < 1.5$ clusters from the *Spitzer*/IRAC Shallow Cluster Survey (ISCS; E08). This large statistical sample—consisting of 196 spectroscopic cluster members at $z > 1$ including 91 at $z > 1.35$, supplemented by robust photo- z members for complete sampling—allows accurate mean cluster properties to be determined, overcoming shot noise due to low numbers of objects in individual cluster cores and systematic variations in star formation history. We use $24 \mu\text{m}$ *Spitzer* data to directly probe the obscured star formation largely missed by optical approaches, and we reject contaminating active galactic nuclei (AGNs) by using both X-ray and mid-IR methods.

In Section 2 we describe the ISCS cluster sample as well as the extensive photometry, spanning X-ray to $24 \mu\text{m}$ wavelengths, that is available for all of these clusters. We describe the uniform photometric redshifts used to identify these clusters, and we present spectroscopy for six newly confirmed $z > 1$ clusters, five of which are at $z > 1.35$. Calculations of stellar masses, total IR luminosities, and SFRs are described in Section 3. Cluster membership criteria and AGN rejection methods are described in Section 4. In Section 5, the SFR and sSFR in the ISCS clusters are presented, and the implications for cluster formation are discussed in Section 6. We present our conclusions in Section 7. We use Vega magnitudes, the Chabrier (2003) initial mass function (IMF), and the Wilkinson Microwave Anisotropy Probe 7 cosmology of $(\Omega_\Lambda, \Omega_M, h) = (0.728, 0.272, 0.704)$ of Komatsu et al. (2011).

2. DATA

2.1. IRAC Shallow Cluster Survey

The ISCS (E08) is a wide-field IR-selected galaxy cluster survey carried out using the *Spitzer*/IRAC Shallow Survey imaging (Eisenhardt et al. 2004) of the 8.5 deg^2 Boötes field of the NOAO Deep, Wide-Field Survey (NDWFS; Jannuzi & Dey 1999). The clusters are identified via a wavelet search algorithm operating on photometric redshift probability distribution functions for $4.5 \mu\text{m}$ selected galaxies in thin redshift slices over the redshift range $0 < z < 2$. The ISCS sample contains 335 clusters and groups in an area of 7.25 deg^2 , 106 of which are at $z > 1$.

Details of the photometric redshifts are given in Brodwin et al. (2006, hereafter B06), and a full description of the cluster search and spectroscopy for a dozen $z > 1$ ISCS clusters is given in E08 (also see Stanford et al. 2005; B06; Elston et al. 2006). In Brodwin et al. (2011) we presented our most distant cluster at that time, ISCS J1432.4+3250 at $z = 1.49$, though a new, deep extension to the survey has thus far identified two more distant clusters at $z = 1.75$ (Stanford et al. 2012; Brodwin et al. 2012; Gonzalez et al. 2012) and $z = 1.89$ (Zeimann et al. 2012).

Here we focus on 16 ISCS clusters at $1 < z < 1.5$, listed in Table 1, that have deep multi-wavelength follow-up observations from the X-ray to mid-IR methods and are spectroscopically confirmed. These clusters likely all have similar halo masses, in the range $\sim (0.8\text{--}2) \times 10^{14} M_\odot$. This statement is based on X-ray, weak lensing, and dynamical masses that have been measured for a subset of them (Brodwin et al. 2011; Jee et al. 2011), as well as on a clustering analysis of the full ISCS sample (Brodwin et al. 2007). In a companion paper, Alberts et al. (2013) conduct a *Herschel*/SPIRE stacking analysis using the full ISCS catalog.

2.2. New $z > 1$ ISCS Clusters

Six new $z > 1$ ISCS clusters spanning $1.157 < z < 1.464$ have been spectroscopically confirmed using a combination of multi-object Keck optical spectroscopy and slitless NIR grism spectroscopy using the Wide Field Camera 3 (WFC3) on *Hubble Space Telescope* (HST). A few additional members were confirmed in the AGES survey (Kochanek et al. 2012). Table 2 lists the coordinates, observation dates, exposure times, and redshifts for previously unpublished members identified via ground-based optical spectroscopy. The new members identified via IR HST/WFC3 grism observations, also used in this analysis, are presented in Zeimann et al. (2013).

The Keck optical spectra were reduced using standard techniques, including flat fielding, fringe correction for LRIS red-side spectra, cosmic ray rejection, wavelength calibration, and stacking. Spectral features were identified in the one-dimensional spectra extracted in IRAF,¹⁵ although all identified emission lines were verified to be robust in the two-dimensional spectra. Redshifts for star-forming galaxies were determined from a combination of $[\text{O}\,\text{II}] \lambda 3727$ emission and the 4000\AA break or overall spectral shape, whereas redshifts for passive galaxies were secured primarily via Ca H and K absorption lines.

Optical/IRAC pseudocolor images of these new clusters, with the spectroscopic members indicated, are shown in Figure 1. Although prominent red overdensities are present for most of the clusters, the ISCS clusters are not red-sequence selected. The photometric redshift methodology includes bluer members, as is evident in some of the panels of Figure 1, and therefore offers a selection that is less biased toward red-and-dead membership than simple red-sequence surveys. This is of crucial importance for studies of the star formation activity in high-redshift clusters.

2.3. Photometry and Photometric Redshifts

2.3.1. Optical and IRAC Data

Deep, optical B_{WRI} data from the NDWFS (Jannuzi & Dey 1999) are available for all of these clusters (see B06 for more details). In order to match the larger point-spread

¹⁵ IRAF is distributed by the National Optical Astronomy Observatory, which is operated by the Association of Universities for Research in Astronomy (AURA) under cooperative agreement with the National Science Foundation.

Table 1
High-redshift, Multiwavelength ISCS Cluster Sample

ID	R.A. (J2000)	Decl. (J2000)	Spectroscopic Redshift	Number of Spectroscopic Members ^a	Additional References
ISCS J1429.2+3357	14:29:15.16	+33:57:08.5	1.059	8	1, 2
ISCS J1432.4+3332	14:32:29.18	+33:32:36.0	1.113	26	1, 2, 3
ISCS J1426.1+3403	14:26:09.51	+34:03:41.1	1.135	12	1, 2
ISCS J1425.0+3520 ^b	14:25:03.44	+35:20:10.4	1.157	8	—
ISCS J1426.5+3339	14:26:30.42	+33:39:33.2	1.164	14	1, 2
ISCS J1434.5+3427	14:34:30.44	+34:27:12.3	1.238	19	1, 2, 4
ISCS J1429.3+3437	14:29:18.51	+34:37:25.8	1.261	18	1, 2
ISCS J1432.6+3436	14:32:38.38	+34:36:49.0	1.351	12	1, 2
ISCS J1425.3+3428 ^b	14:25:19.33	+34:28:38.2	1.365	14	2
ISCS J1433.8+3325 ^b	14:33:51.14	+33:25:51.1	1.369	6	2
ISCS J1434.7+3519	14:34:46.33	+35:19:33.5	1.374	10	1, 2
ISCS J1432.3+3253 ^b	14:32:18.31	+32:53:07.8	1.395	10	2
ISCS J1425.3+3250 ^b	14:25:18.50	+32:50:40.5	1.400	6	2
ISCS J1438.1+3414	14:38:08.71	+34:14:19.2	1.414	16	1, 2, 5, 6
ISCS J1431.1+3459 ^b	14:31:08.06	+34:59:43.3	1.463	6	2
ISCS J1432.4+3250	14:32:24.16	+32:50:03.7	1.487	11	2, 6

Notes.

^a See Section 4 for the definition of cluster membership.

^b New spectroscopic confirmation in this work.

References. (1) E08; (2) Zeimann et al. 2013; (3) Elston et al. 2006; (4) B06; (5) Stanford et al. 2005; (6) Brodwin et al. 2011.

functions (PSFs) of the *Spitzer*/IRAC photometry described below, aperture-corrected 4'' aperture fluxes were used.

The original 90 s depth IRAC Shallow Survey was repeated three more times as part of the *Spitzer* Deep, Wide-Field Survey (SDWFS; Ashby et al. 2009) in *Spitzer* Cycle 4 (PID 40839), leading to a factor of two increase in depth and a significantly more robust catalog in terms of resistance to cosmic rays and instrumental effects. Combined with new, PSF-matched NDWFS optical catalogs (M. J. I. Brown et al., in preparation), these data were used to compute new photometric redshifts for the full 5 σ 4.5 μ m SDWFS sample consisting of 434,295 galaxies down to an aperture-corrected limit of [4.5] = 18.83 mag.

2.3.2. MIPS Data

Imaging at 24 μ m was obtained with the Multiband Imaging Photometer for *Spitzer* (MIPS) in Cycle 3 (PID 30950) for all the clusters in Table 1. The exposure time increased with redshift from 12 to 48 minutes, corresponding to rms flux limits of 52 μ Jy at $z = 1$ to 12 μ Jy at $z = 1.5$, in order to uniformly detect $3 \times 10^{11} L_{\odot}$ LIRGs at signal-to-noise ratio (S/N) ≥ 4 for all clusters in this sample.

Following generation of the BCD by the *Spitzer* Science Center pipeline, we flat-fielded our images using scan mirror position-dependent flat fields derived from our science data. This is necessary because MIPS flat fields are slightly dependent on the position of scan mirrors.¹⁶ We also performed a jailbar correction on some science data that presented a regular pattern of bars (due to the presence of saturated pixels). The images were then sky-subtracted and the final mosaics were produced by using MOPEX (with a drizzle scale of 0.7 and a pixel-resampling factor of two).

The MIPS data have an angular resolution of 5''.7 FWHM, while the relative astrometric accuracy derived by matching the

24 μ m sources with Two Micron All Sky Survey stars and the SDWFS IRAC images is better than 0''.25. The sources discussed in this paper are all unresolved at MIPS resolution; most are unresolved even at IRAC resolution. The MIPS source catalogs were generated by using the positions of sources in the higher resolution IRAC images and fitting groups of point sources by using a singular value decomposition technique at the positions of the IRAC sources to minimize the effect of source confusion. This is equivalent to a DAOPHOT-type approach (Stetson 1987), which is commonly adopted to obtain stellar photometry in crowded fields.

2.3.3. Chandra X-Ray Data

Several of these cluster positions had been previously imaged with *Chandra* to 5–15 ks depths (Murray et al. 2005). A Cycle 10 *Chandra* program added additional exposure time to bring the full sample to a uniform exposure time of 40 ks. Although the shallow X-ray exposures were designed to study bright AGNs, emission from the ICM is detected for several of them. A complete description of the reduction of these data, along with ICM mass measurements for two $z > 1.4$ clusters in the present sample, is given in Brodwin et al. (2011).

2.3.4. Matched Catalogs

The various analyses in this work are based on cluster galaxy samples selected in IRAC and/or MIPS bands from the global 4.5 μ m limited photometric redshift catalog described above. Photometric redshift and stellar mass fits use the optical and IRAC bands, with uniform 4'' aperture fluxes measured at the positions of the SDWFS 4.5 μ m sources. Unlike in B06, the optical images were first convolved to a uniform 1''.35 PSF to produce more robust optical colors and to better match the native IRAC PSF. All photometry was corrected to total flux by using a curve of growth analysis on bright, unsaturated stars. Since the SDWFS 4.5 μ m catalog was used as a positional prior to extract 24 μ m fluxes in the MIPS images (e.g., Magnelli

¹⁶ See <http://irsa.ipac.caltech.edu/data/SPITZER/docs/mips/features/> for details.

Table 2
Spectroscopic Cluster Members^a

ID	R.A. (J2000)	Decl. (J2000)	Spec- z	Instrument	UT Date	Exposure Time (s)
ISCS_J1425.0+3520 (z) = 1.157						
J142503.5+352013	14:25:03.58	+35:20:13.4	1.1570	Hectospec	AGES ^b	AGES ^b
J142504.6+352114	14:25:04.62	+35:21:14.1	1.1572	LRIS	2009 Apr 28	6 × 1800 s
J142505.7+352248	14:25:05.73	+35:22:48.3	1.156	LRIS	2009 Apr 28	6 × 1800 s
J142507.4+351902	14:25:07.42	+35:19:02.4	1.157	LRIS	2009 Apr 28	6 × 1800 s
J142507.6+352151	14:25:07.61	+35:21:51.2	1.154	LRIS	2009 Apr 28	6 × 1800 s
J142510.7+352315	14:25:10.72	+35:23:15.0	1.1588	LRIS	2009 Apr 28	6 × 1800 s
J142512.0+351839	14:25:12.00	+35:18:39.1	1.157	LRIS	2009 Apr 28	6 × 1800 s
J142512.1+351955	14:25:12.18	+35:19:55.2	1.1449	LRIS	2009 Apr 28	6 × 1800 s
ISCS_J1426.5+3339 (z) = 1.164						
J142619.7+333717	14:26:19.74	+33:37:17.0	1.165	LRIS	2012 Apr 20	3 × 1140 s
J142631.2+334307	14:26:31.20	+33:43:07.1	1.160	LRIS	2012 Apr 20	3 × 1140 s
J142633.4+334224	14:26:33.46	+33:42:24.5	1.160	LRIS	2012 Apr 20	3 × 1140 s
ISCS_J1425.3+3428 (z) = 1.365						
J142511.3+342852	14:25:11.31	+34:28:52.8	1.3759	LRIS	2006 Apr 5	7 × 1760 s
J142516.0+343040	14:25:16.02	+34:30:40.9	1.39	LRIS	2006 Apr 5	7 × 1760 s
J142519.0+342807	14:25:19.05	+34:28:07.2	1.3574	LRIS	2006 Apr 5	7 × 1760 s
ISCS_J1433.8+3325 (z) = 1.369						
J143333.9+332602	14:33:33.98	+33:26:02.9	1.377	DEIMOS	2007 Apr 19	4 × 1800 s
J143351.5+332645	14:33:51.55	+33:26:45.9	1.3687	Hectospec	AGES ^b	AGES ^b
J143349.0+332603	14:33:49.05	+33:26:03.3	1.39	LRIS	2006 Apr 4	7 × 1740 s
ISCS_J1432.3+3253 (z) = 1.395						
J143211.5+325646	14:32:11.56	+32:56:46.7	1.401	LRIS	2012 Apr 20	4 × 1740 s
J143216.5+325433	14:32:16.54	+32:54:33.9	1.3921	Hectospec	AGES ^b	AGES ^b
ISCS_J1425.3+3250 (z) = 1.400						
J142523.8+325001	14:25:23.85	+32:50:01.7	1.41	LRIS	2012 Apr 20	4 × 1740 s
J142520.3+324701	14:25:20.34	+32:47:01.7	1.3972	Hectospec	AGES ^b	AGES ^b
ISCS_J1431.1+3459 (z) = 1.463						
J143110.8+350016	14:31:10.88	+35:00:16.4	1.477	LRIS	2012 Apr 21	4 × 1740 s
ISCS_J1432.4+3250 (z) = 1.487						
J143225.1+325013	14:32:25.15	+32:50:13.6	1.49	LRIS	2012 Apr 20	4 × 1740 s
J143225.1+325010	14:32:25.18	+32:50:10.4	1.491	LRIS	2012 Apr 20	4 × 1740 s

Notes.

^a Only previously unpublished redshifts from ground-based telescopes are included. See the Table 1 references for previously published members. Additional new redshifts obtained with the *HST*/WFC3 grism are presented in a companion paper (Zeimann et al. 2013).

^b See Kochanek et al. (2012) for a complete description of the AGES spectroscopy.

et al. 2009), IR luminosities (L_{IR}) or limits are measured for all sources.

2.3.5. Photometric Redshifts

The photometric redshift methodology adopted here is broadly similar to that of B06, with the main difference being that with the greater SDWFS depth the 5.8 and 8.0 μm catalogs are included because they are sensitive to nonlocal galaxy populations. The extended Coleman et al. (1980) and Kinney et al. (1996) templates used in B06 do not sample these wavelengths, so in this work the models of Polletta et al. (2007) were adopted. Specifically, the templates employed include Ell5, Ell13, S0, Sa, Sb, Sc, Sd, Spi4, and M82. This subset of the Polletta et al. (2007) templates, supplemented by the extended Coleman et al. (1980) elliptical template, were empirically determined to provide an excellent spectral basis for SDWFS galax-

ies at $0 < z < 2$ (i.e., spanning the rest-frame wavelengths of $\sim 0.1\text{--}8 \mu\text{m}$ probed by our filters).

The accuracy and precision of the new photometric redshifts are very similar to those described in B06, with $\sigma/(1+z) \approx 0.06$ for 95% of the galaxies. The key improvement is that the photo- z sample now extends to the SDWFS 5 σ survey limit, corresponding to $0.22 L^*$ at $z = 1.5$. Unlike in B06, a neural-net approach was not attempted for the bright AGNs as these are identified and removed using our complementary data, as described below. Figure 2 shows the quality of the photometric redshifts for galaxies on lines of sight toward the 16 clusters in Table 1. The slight bias to higher photometric redshifts evident at $z \lesssim 0.5$ was not corrected as the present focus is on $z > 1$ galaxies. Larger filled-in circles represent galaxies detected at $S/\text{N} \geq 4$ in the $24 \mu\text{m}$ MIPS band, to which the rest of the discussion in this paper will be limited. Both the full and MIPS-detected line-of-sight galaxy populations

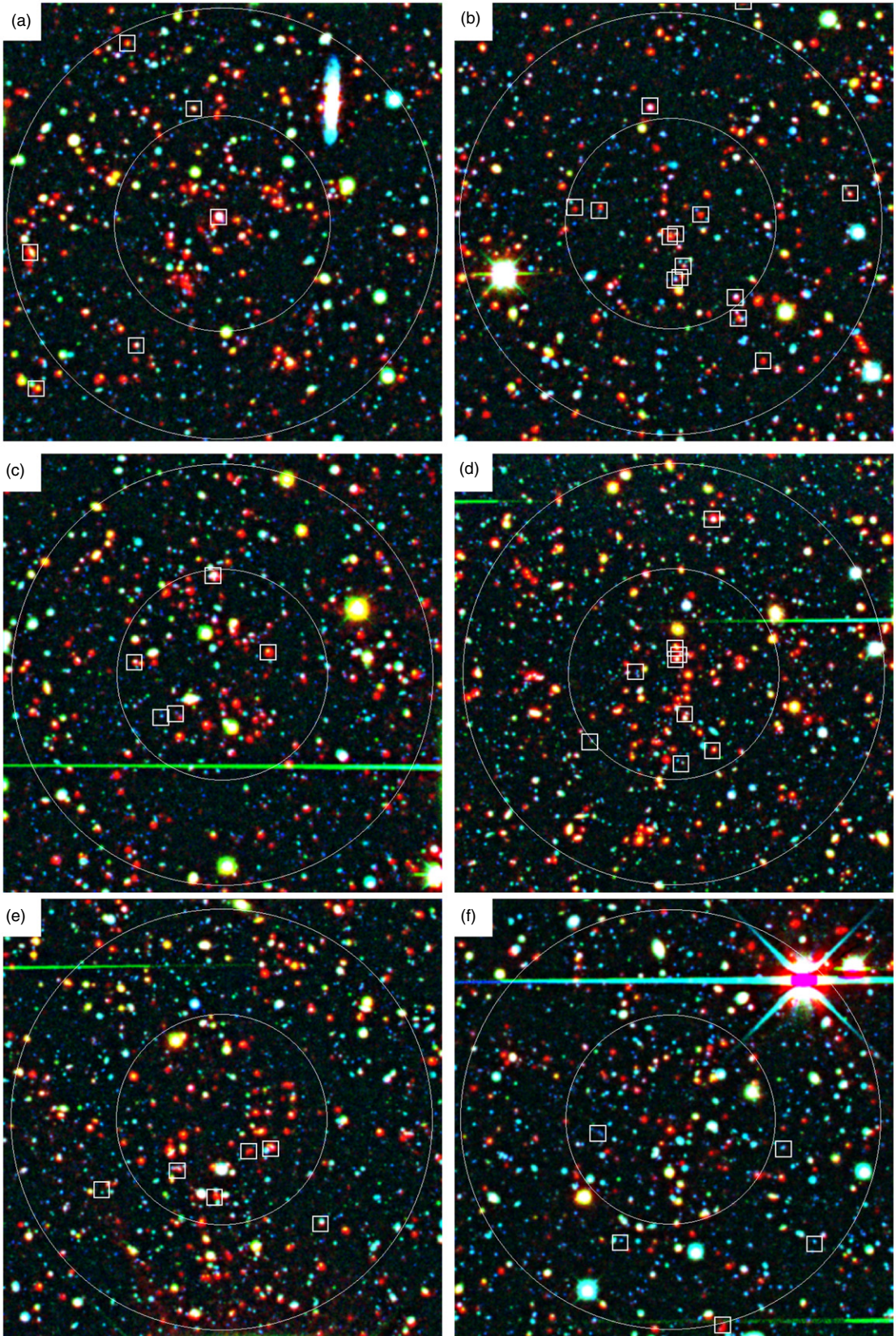


Figure 1. $4'1 \times 4'1$ optical B_W , I , and IRAC $4.5 \mu\text{m}$ pseudocolor images of six high-redshift clusters newly spectroscopically confirmed in this work. The large circles denote radii of 0.5 and 1 Mpc and are centered on the wavelet detection centroids. The white boxes indicate spectroscopic members; some spectroscopic members at radii between 1 and 2 Mpc are not shown. (a) ISCS J1425.0+3520 at $\langle z_{\text{sp}} \rangle = 1.157$; (b) ISCS J1425.3+3428 at $\langle z_{\text{sp}} \rangle = 1.365$; (c) ISCS J1433.8+3325 at $\langle z_{\text{sp}} \rangle = 1.369$; (d) ISCS J1432.3+3253 at $\langle z_{\text{sp}} \rangle = 1.395$; (e) ISCS J1425.3+3250 at $\langle z_{\text{sp}} \rangle = 1.400$; and (f) ISCS J1431.1+3459 at $\langle z_{\text{sp}} \rangle = 1.463$. The color image for the last cluster is made up of B_W , R , and IRAC $4.5 \mu\text{m}$.

(A color version of this figure is available in the online journal.)

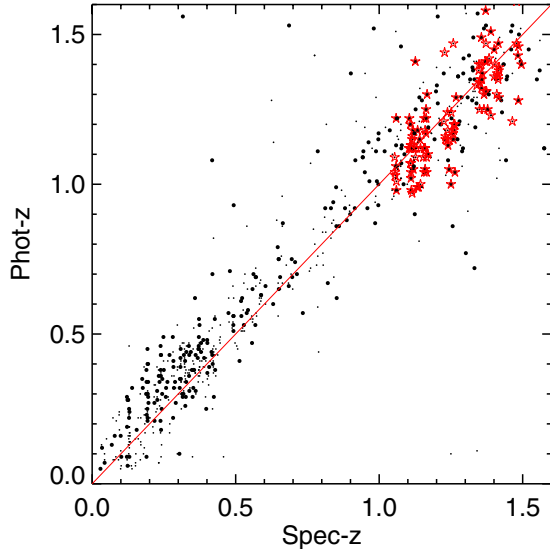


Figure 2. Photometric redshift accuracy toward the 16 high- z clusters in Table 1. AGNs have been removed as described in Section 4.2. Larger symbols are MIPS-detected; the dispersion for this sample is the same as for the general galaxy population. The stars are $z > 1$ spectroscopic cluster members.

(A color version of this figure is available in the online journal.)

Sample	Confidence Level Statistics ^a		
	$<1\sigma$	$<2\sigma$	$<3\sigma$
Gaussian expectation	68.3%	95.4%	99.7%
SDWFS main galaxy sample	73.8%	96.5%	99.3%
This work	74.6%	93.6%	98.6%
This work $z > 1$	81.1%	93.0%	98.7%

Note. ^a Percentage of galaxies for which the spectroscopic redshift falls within the 1σ , 2σ , and 3σ photometric redshifts confidence intervals.

have redshift dispersions similar to the full field, $\sigma/(1+z) = 0.064$ and 0.069 , respectively. Spectroscopically confirmed cluster members, denoted by stars, have a significantly tighter dispersion, $\sigma/(1+z) = 0.039$.

As a further test of the reliability of the photometric redshifts, Table 3 shows the fraction of galaxies for which the spectroscopic redshift lies within the 1σ , 2σ , and 3σ confidence intervals, defined as the redshift regions that enclose the top 68.3%, 95.4%, and 99.7% of the normalized area under the photometric redshift probability distributions. The photometric redshift accuracy in these clusters fields is as good as or better than that of the general SDWFS sample, particularly for the $z > 1$ galaxies that form the basis of this work.

3. STELLAR MASSES, TOTAL LUMINOSITIES, AND STAR FORMATION RATES

We estimate stellar masses by using iSEDfit (Moustakas et al. 2013), a Bayesian spectral energy distribution (SED) fitting code that uses population synthesis models to infer the physical properties of a galaxy given its observed broadband SED. We adopt the Bruzual & Charlot (2003) population synthesis models based on the Padova isochrones, the STELIB (Le Borgne et al. 2003) stellar library, and the Chabrier (2003) IMF ranging from 0.1 to $100 M_{\odot}$. The upper panel of Figure 3 shows the stellar masses of all galaxies along the line of sight to these clusters. For uniformity across the $1 < z < 1.5$ cluster sample, we restrict the stellar masses to $\log(M_{\star}/M_{\odot}) \geq 10.1$. This limit corresponds

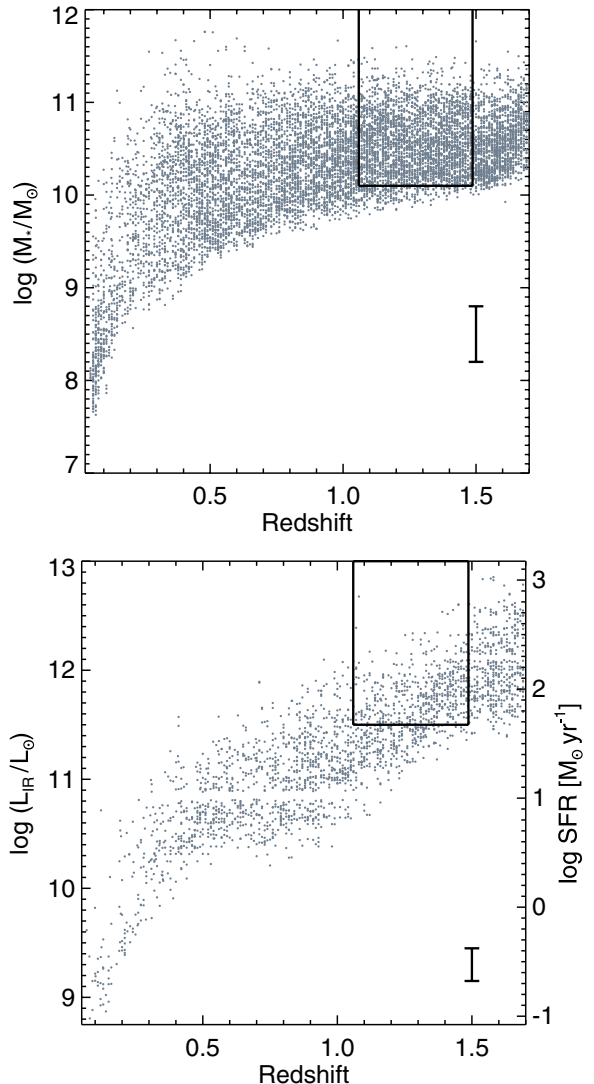


Figure 3. Upper panel: stellar masses along $5' \times 5'$ lines of sight to the high-redshift clusters. The selection region is enclosed by the box, corresponding to a stellar mass limit of $\log(M_{\star}/M_{\odot}) \geq 10.1$ for a Chabrier IMF. Lower panel: IR luminosities in the same fields, with sampling complete to $\log(L_{\text{IR}}/L_{\odot}) \geq 11.5$. The redshifts in both panels are predominantly photometric. The error bars are described in the text.

to the $\sim 80\%$ completeness level, though our cluster member completeness is far higher over this redshift range given the high masses of cluster galaxies and the flat luminosity function (Mancone et al. 2012). Although the individual iSEDfit mass errors are typically ≤ 0.2 dex, we adopt an error floor of 0.3 dex (indicated by the error bar in the figure) to account for the systematic uncertainty inherent in mass fitting.

The total IR luminosities of these galaxies are inferred from the $24 \mu\text{m}$ fluxes by using the Chary & Elbaz (2001) templates. While this tends to overestimate L_{IR} at high redshift ($z > 1.5$), particularly for AGN-dominated ULIRGs (Murphy et al. 2009; Nordon et al. 2010; Rodighiero et al. 2010), it provides an accurate (scatter $\sim 40\%$) estimate of L_{IR} out to $z = 1.5$ (Marcillac et al. 2006; Murphy et al. 2009; Elbaz et al. 2010). The MIPS data allow a complete sample of total IR luminosities down to $L_{\text{IR}} = 10^{11.5} L_{\odot}$ for all our clusters (lower panel of Figure 3), and we adopt this as the selection limit. The horizontal gap visible as a lack of sources with $L_{\text{IR}} \approx 10^{10.85} L_{\odot}$ is an artifact stemming from the discreteness of the Chary & Elbaz

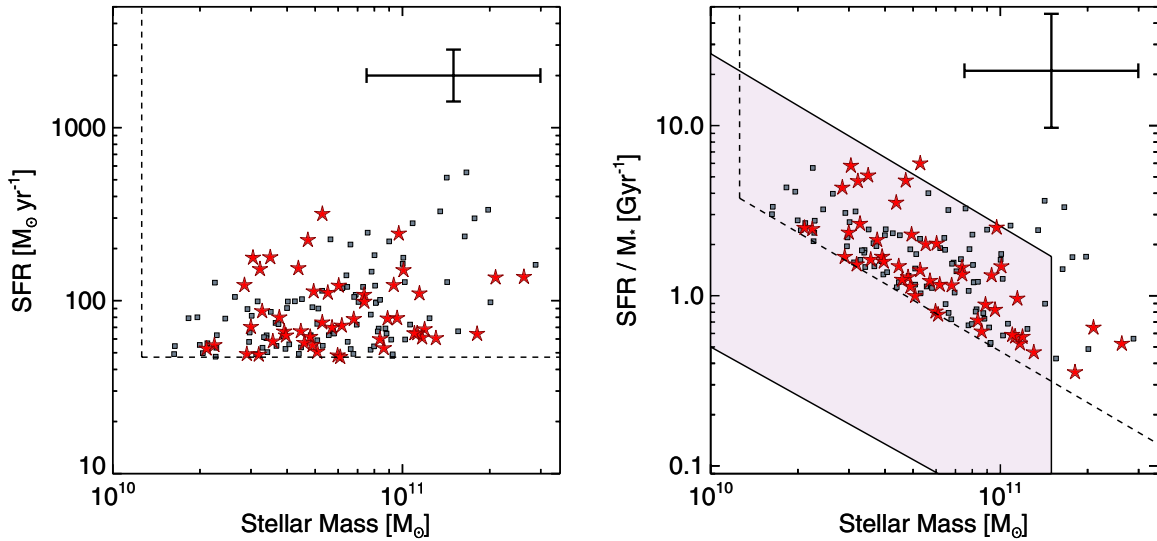


Figure 4. Star formation (left panel) and specific star formation rates (right panel) vs. stellar mass for the high-redshift cluster sample for galaxies detected at $24\mu\text{m}$ with $\text{S/N} \geq 4$. The squares and stars represent photometric and spectroscopic redshift members, respectively. The large error bars indicate the systematic uncertainties. For comparison, the shaded region indicates the sSFR properties of the field galaxy sample of Santini et al. (2009). The dashed lines delineate the selection limits in stellar mass, SFR, and sSFR.

(A color version of this figure is available in the online journal.)

(2001) templates. Given our selection region, it does not affect the present analysis. The scatter is indicated by the error bar in the figure. We convert the total IR luminosities to SFRs using the relation given in Murphy et al. (2011). This is defined assuming a Kroupa (2001) IMF and therefore has a similar normalization to the Chabrier IMF used to calculate our stellar masses.

The primary goals of this paper are to compare the SFR and sSFR in the cluster outskirts and cores and between clusters and the field. In all cases these SFRs have been derived using the same templates, so these comparisons should be robust to small absolute deviations in SFR compared with measurements at longer wavelengths (i.e., with *Herschel*).

4. CLUSTER MEMBERSHIP

4.1. Identification of Members

Following E08, galaxies with robust spectroscopic redshifts are identified as likely cluster members if they lie within a radius of 2 Mpc and their relative velocities are within 2000 km s^{-1} of the systemic cluster velocity. Galaxies without spectroscopy are identified as cluster members via a constraint on the integral of their normalized photometric redshift probability distribution functions:

$$\int_{z_{\text{cl}} - 0.06(1+z_{\text{cl}})}^{z_{\text{cl}} + 0.06(1+z_{\text{cl}})} P(z) dz \geq 0.3, \quad (1)$$

where z_{cl} is the best-fit photometric redshift of the cluster, determined by iteratively summing up the $P(z)$ functions for member galaxies within 1 Mpc , reidentifying members, and repeating the process to convergence. The positional centers are taken from the wavelet algorithm used to initially identify the clusters, although we have verified that using the brightest cluster galaxy (BCG) position yields similar results.

4.2. Rejection of AGNs

AGNs are problematic to include in this analysis because of the difficulty of obtaining good photometric redshifts for them and because they bias the SFRs inferred from the IR luminosity. We therefore choose to omit them with the understanding that the

resulting SFRs are formally lower limits. X-ray-emitting AGN with $2\text{--}10\text{ keV}$ luminosities brighter than $L_X > 10^{43}\text{ erg s}^{-1}$ were identified via a positional match to the matched catalog, within a match radius that is the larger of the IRAC PSF ($\approx 1.7''$) and the *Chandra* positional uncertainty (which varies with off-axis angle). We also identify AGNs via their power law emission in the IRAC bands. Objects with $\text{S/N} \geq 5$ in all four IRAC bands that fall in the Stern et al. (2005) AGN wedge were deemed AGNs. Objects satisfying either of these AGN criteria are removed from this analysis.

We have verified that the rejected AGNs represent a relatively small fraction of our cluster membership and have no strong redshift dependence, as this could bias our primary result. Only $\sim 4\%$ of members satisfying our stellar mass cut are rejected as AGNs within a radius of 1 Mpc , with no apparent redshift trend (2.8%, 6.0%, and 4.1% in the three redshift bins used in Section 5). Similarly, of the subset of members that are detected at $24\mu\text{m}$, only $\sim 12\%$ are rejected as AGNs (11.1%, 15.3%, and 9.9% in these redshift bins). In the cluster cores, within projected radii of 0.5 Mpc , the rejected fractions are slightly higher ($\sim 7\%$ and $\sim 18\%$ for all and for $24\mu\text{m}$ detected members, respectively), but there is still no trend with redshift. As we reject more AGNs in the cores, we may possibly be underestimating the SFR in the cores relative to the outskirts at all redshifts. Since our results actually go the other way, with higher activity in the cores, we conclude that the rejection of AGNs does not significantly bias our results with respect to SFR trends in redshift or radius.

5. STAR FORMATION IN HIGH-REDSHIFT CLUSTERS

5.1. $24\mu\text{m}$ Detected Cluster Members

Figure 4 shows the SFR (left panel) and sSFR (right panel) as a function of stellar mass for galaxies above the stellar mass and L_{IR} limits given in Section 3. The small boxes are galaxies satisfying the cluster membership criteria defined in Section 4, and the stars indicate galaxies for which cluster membership has been spectroscopically confirmed. The large error bars indicate the systematic errors. For the stellar masses,

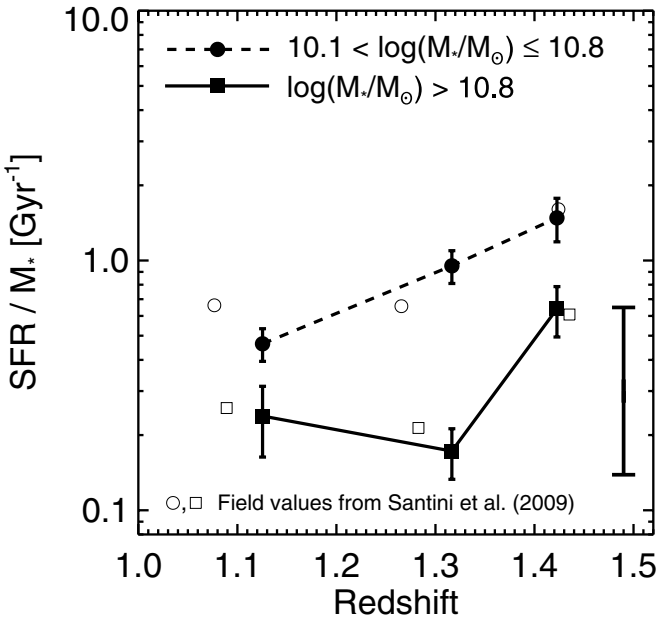


Figure 5. Mean sSFR of central cluster galaxies, within projected radii of 500 kpc, in bins of stellar mass and redshift. The errors on the points are from bootstrap resampling the galaxies in each bin, and the large error bar at right indicates the systematic uncertainty in the sSFR. For comparison, the open symbols show the sSFR the field galaxy sample of Santini et al. (2009) in the same mass and redshift bins.

these are conservatively estimated to be 0.3 dex, accounting for IMF variations (e.g., Bell et al. 2003). For the SFRs, the systematic error is taken to be 40% on the basis of a comparison with *Herschel* far-IR measurements (Elbaz et al. 2010).

The region of the sSFR plot populated by the field galaxy sample of Santini et al. (2009) at $1 < z < 1.5$, adjusted to our choice of IMF, is shown for comparison. The MIPS data for this small field survey are much deeper and hence probe to lower SFR. However, to our SFR sensitivity limit the cluster members, both spectroscopic and photometric, have sSFRs very similar to these field galaxies. The spectroscopically confirmed cluster members span a similar range in stellar mass, SFR and sSFR as the photometric redshift members. Given the small photometric redshift error for cluster members (Section 2.3.5), the integrated cluster SFR measurements, using spectroscopic redshifts where available and photometric redshifts otherwise, should be robust.

5.2. Star Formation versus Stellar Mass and Redshift

The mean sSFR of the central cluster galaxies, within projected radii of 500 kpc, are plotted in Figure 5 in bins of stellar mass and redshift. The mean sSFR is defined here as the sum of the SFRs divided by the sum of the stellar masses in the mass bin. Objects undetected above 4σ at $24 \mu\text{m}$ in any bin are assigned the median $24 \mu\text{m}$ flux of all such formally undetected objects in that bin. This catalog-space median stacking is complementary to the more common image-space stacking employed in a companion paper (Alberts et al. 2013). We have verified that none of the main results in this work depend on the flux we infer for the undetected sources—our primary conclusions are unchanged if the fluxes of all galaxies with $\text{S/N} < 4\sigma$ MIPS detections are set to zero. For comparison, we plot the sSFR of field galaxies from Santini et al. (2009, open symbols) in the same mass bins. In this field study, SFRs

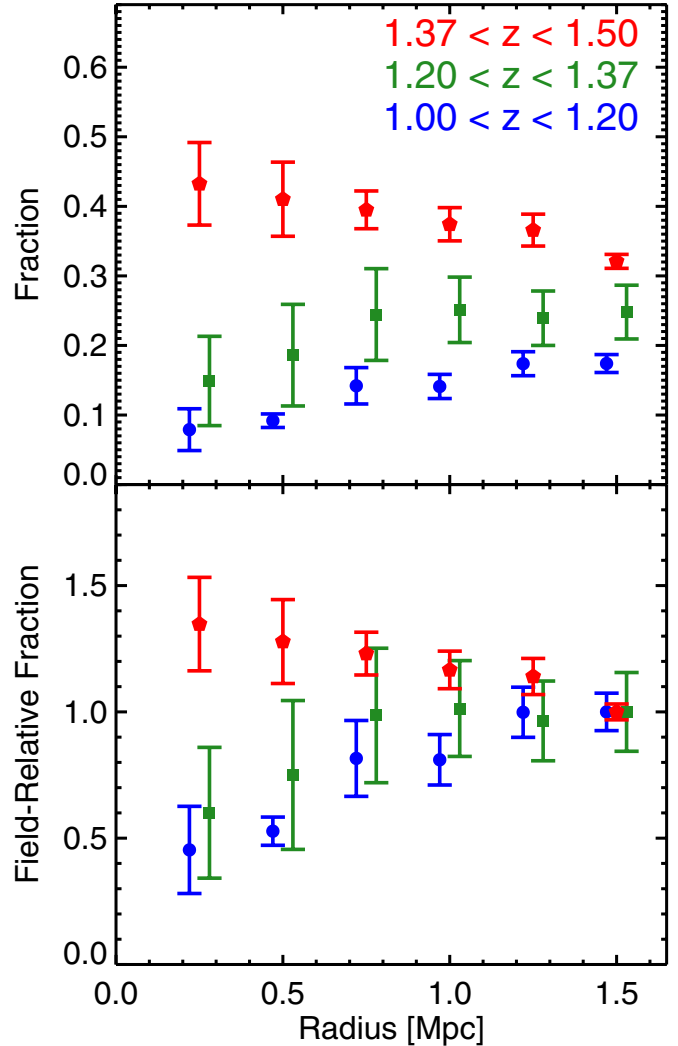


Figure 6. Upper panel: relative fraction of star-forming cluster members with $L_{\text{IR}} \geq 10^{11.5} L_{\odot}$ vs. projected clustercentric radius for members with $\log(M_{\star}/M_{\odot}) \geq 10.1$. Lower panel: field-relative fractions, where the field fractions are taken to be the values at a radius of 1.5 Mpc.
(A color version of this figure is available in the online journal.)

for galaxies undetected at $24 \mu\text{m}$ are calculated from opt/NIR SED fits.

Although the methodologies differ in detail, the cluster and field samples share some key characteristics. The cluster galaxies appear to lie in the same region of the sSFR–stellar mass plane as do the star-forming field galaxies. Similarly, the same evolutionary trend is apparent in both cluster and field samples, with the sSFR increasing over $1 < z < 1.5$. The increase appears to be particularly rapid for the more massive cluster galaxies above $z \gtrsim 1.3$, perhaps indicating that vigorous star formation is occurring in the massive central galaxies in these clusters at levels comparable to the field.

5.3. Star Formation versus Radius and Redshift

To probe the effect of environment on star formation in $z > 1$ clusters, we plot in Figure 6 (upper panel) the fraction of cluster members with $L_{\text{IR}} \geq 10^{11.5} L_{\odot}$ versus projected clustercentric radius. The sample is divided into three redshift bins, chosen to have roughly equal numbers of clusters in each bin, and the errors are estimated via bootstrap resampling.

In the lowest redshift bin ($1.0 < z < 1.2$), the LIRG fraction within r_{200} is roughly consistent with that seen at $z \sim 0.8$ by Finn et al. (2010) in the ESO Distant Cluster Survey (White et al. 2005), although that work probes to lower IR luminosities ($\sim 10^{11} L_\odot$). At the other extreme, the most distant ISCS clusters have a LIRG fraction similar to, or even somewhat higher than, IR-selected cluster CIG J0218.3–0510 at $z = 1.62$ (Tran et al. 2010). However, as demonstrated below, there is significant cluster-to-cluster variation in star formation properties, so comparisons of individual clusters should be interpreted with caution.

For the ISCS clusters in the two bins at $z < 1.37$, the fraction of star-forming members drops significantly from a radius of about 1.5 Mpc, which is outside the virial radius ($r_{200} \sim 1$ Mpc) for this sample, to the inner 250 kpc. This is expected because of the quenching of star formation in the central regions of clusters. Indeed, Muzzin et al. (2012) find a very similar star formation radius trend in the GCLASS sample at $z \sim 1$.

However, in the highest redshift bin ($1.37 < z < 1.50$), we find the star-forming fraction does not drop but rather *rises* with decreasing radius right into the cluster cores. This is consistent, in an evolutionary sense, with the observation of Muzzin et al. (2012) that the fraction of post-starburst galaxies in lower-redshift ($z \sim 1$) clusters increases toward the core. Indeed, there is sufficient time between $z \sim 1.5$ and $z \sim 1.0$ (~ 1.5 Gyr) for a significant fraction of the ISCS starbursts to evolve into post-starbursts but only if their star formation is rapidly quenched.

The upper panel of Figure 6 also shows that the fraction of star-forming galaxies in the field, taken here to be the values observed at a radius of 1.5 Mpc, is also increasing with redshift. To better isolate the cluster-specific evolution, the fractions in each redshift bin are normalized to this field value in the lower panel of Figure 6. This plot demonstrates that there is a very clear transition occurring in the cluster galaxies between the highest and middle redshift bins, beyond the global evolution underway in the field. Indeed, the star-forming fraction increases monotonically *from* the field level, rising into the cluster cores.

To better explore the star formation properties as a function of environment, in Figure 7 (upper panel) we plot the SFR surface density versus clustercentric projected radius. There is a strong radial trend, with the SFR surface density increasing by a factor of two to three from the outskirts to the centers of clusters at $1 < z < 1.37$. This is expected even in a quenched environment since the sheer number of galaxies per unit area is increasing toward the cluster cores more rapidly than the SFR is falling.

The SFR surface density trend with radius is considerably more dramatic for clusters in the highest redshift bin ($1.37 < z < 1.50$), where it increases by a factor of ~ 5 , reaching a SFR surface density of nearly $\sim 500 M_\odot \text{ yr}^{-1} \text{ arcmin}^{-2}$ within 250 kpc, i.e., in the cluster cores. Building on the rising star-forming fraction discussed above, this measurement highlights the strong central star formation occurring in clusters at $z \sim 1.5$. We confirm the largely qualitative measurements made on individual, serendipitously discovered clusters at similar redshifts: $z = 1.46$ (Hilton et al. 2010; Hayashi et al. 2011), $z = 1.56$ (Fassbender et al. 2011b), $z = 1.58$ (Santos et al. 2011), and $z = 1.62$ (Tran et al. 2010; Tadaki et al. 2012).

The middle panel of Figure 7 shows the trend of sSFR versus clustercentric radius. In the redshift bins at $1 < z < 1.37$, the sSFR decreases from a level similar to field galaxies in the outskirts (see, e.g., Figure 5) to lower levels toward the center, a drop of a factor of ~ 2 . Although the SFR surface density increases in the cluster cores at these redshifts, the stellar mass

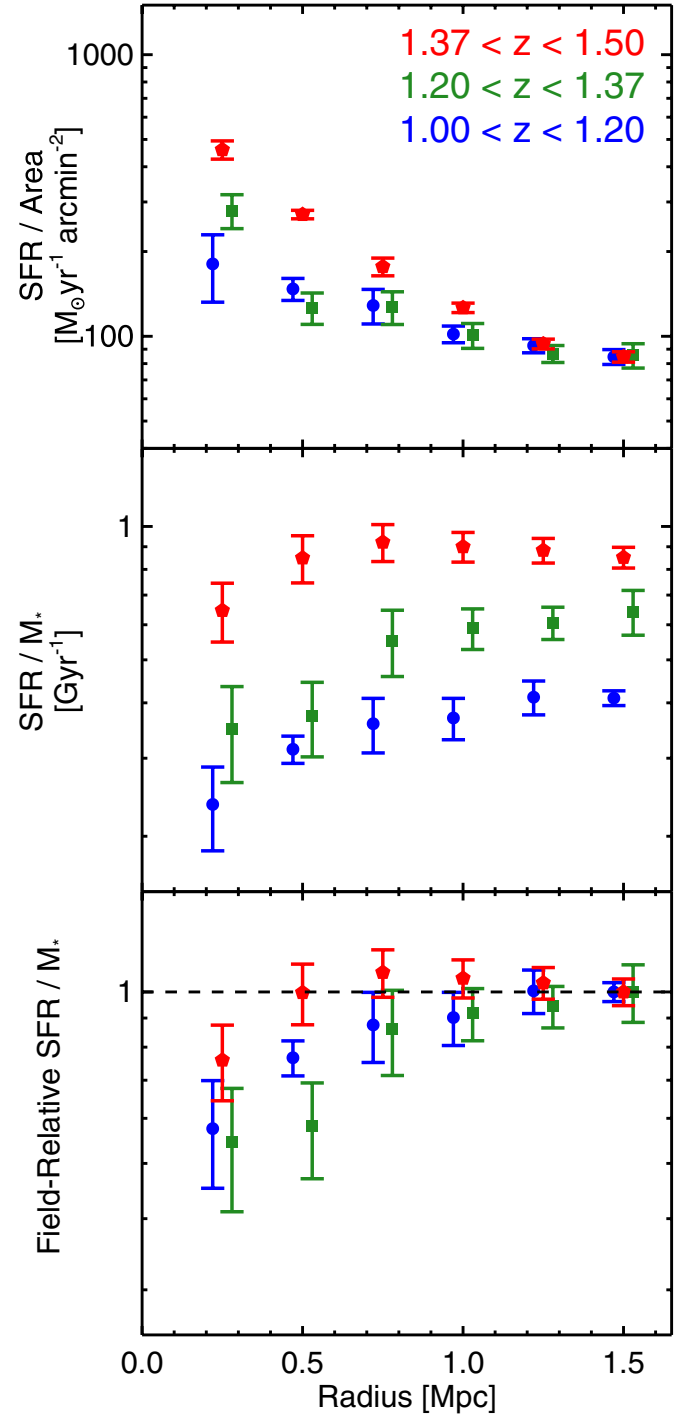


Figure 7. SFR surface density (upper panel) and sSFR (middle panel) vs. projected clustercentric radius for members with $\log(M_*/M_\odot) \geq 10.1$. The errors are from bootstrap resampling. Lower panel: field-relative sSFR, where the field values are taken to be the sSFRs at a radius of 1.5 Mpc. The horizontal line illustrates a model with no environment-dependent quenching.
(A color version of this figure is available in the online journal.)

density is increasing faster, leading to falling sSFR values as in lower redshift clusters, albeit scaled up by a factor of ~ 100 from the local Universe (e.g., Chung et al. 2011).

Conversely, the SFR is increasing so rapidly toward the centers of the clusters in the most distant redshift bin ($1.37 < z < 1.50$) that the sSFR is approximately flat right into the cluster cores. This is the physically crucial transition,

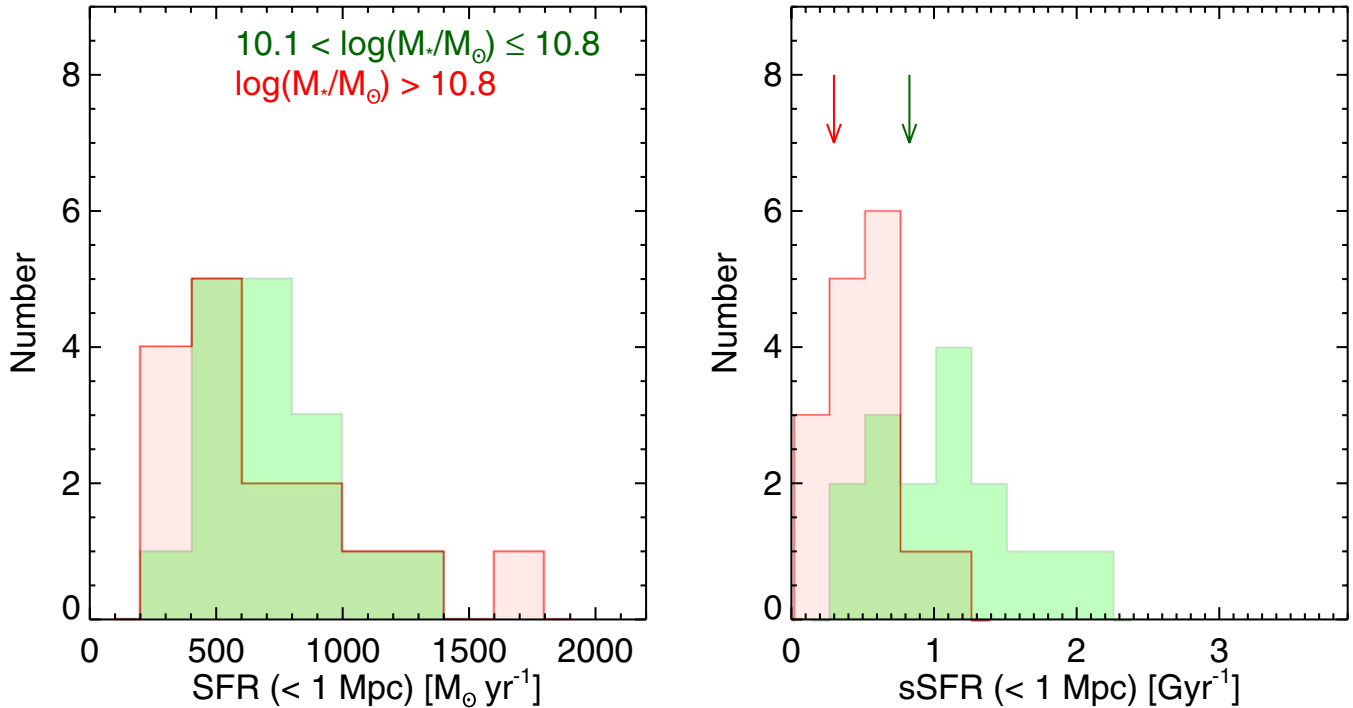


Figure 8. Histograms of the total SFR (left) and sSFR (right) within a projected radius of 1 Mpc, in two bins of stellar mass, showing the cluster-to-cluster variation. The field values of the sSFR in the same mass bins, from Santini et al. (2009), are indicated with arrows.
(A color version of this figure is available in the online journal.)

as it indicates the redshift at which the star formation in recently accreted galaxies has not yet started to be meaningfully quenched. These central cluster galaxies are forming stars as rapidly for their mass as their field galaxy counterparts.

The radial dependence of the sSFRs in all three redshift bins largely reflects that seen in the star-forming fractions in Figure 6. This indicates that this activity is happening across the entire cluster galaxy population, not in just a few star formation-dominated ULIRGs. Indeed, as shown in the lower panel of Figure 3, the bulk of the $24 \mu\text{m}$ detected population are LIRGs that are typical of this redshift regime.

In the lower panel of Figure 7 we plot the field-normalized radial sSFR trend, where the field sSFR in each redshift bin is again taken to be the measurement at a radius of 1.5 Mpc. This removes the strong evolution in field galaxy sSFR and allows a quantitative test of the hypothesis that clusters in the highest redshift bin no longer exhibit environmental quenching. The horizontal line illustrates the expected cluster sSFR in this scenario, identical to the field at all radii. Comparisons of the goodness of fit of this hypothesis to the field-normalized cluster sSFR trends produce χ^2_ν values of 6.50, 5.71, and 1.15 for these sample bins, in order of increasing redshift. Thus, the no-quenching model is ruled out for the lower redshift bins at 4.6σ and 4.2σ , with probability-to-exceed (PTE) values of 4.7×10^{-6} and 2.84×10^{-5} , respectively. Conversely, the high-redshift bin is a satisfactory fit to the no-quenching model, in agreement at the 0.97σ level and corresponding to a PTE of 0.31. Despite this statistical consistency, the sSFR appears slightly depressed in the innermost radius bin, suggesting there may still be a small amount of quenching in the very center, even at this redshift.

5.4. Cluster-to-cluster Variation

The errors that this statistical test rely on are derived from bootstrap resampling the members in each redshift and radius

bin and therefore reflect the scatter due to population variance in each bin. To ensure that the abrupt transition in the highest redshift bin is not due to a single discrepant cluster, we removed each of the six highest redshift clusters in turn and recomputed the central sSFR from the remaining five clusters. The scatter from this jackknife process is smaller than the plotted member-weighted bootstrap errors, confirming that the transition is characteristic of the cluster sample as a whole.

Figure 8 shows histograms in total cluster SFR (left) and sSFR (right) in two mass bins for the 16 clusters in the present sample. The high-mass and low-mass cluster members make similar contributions to the total SFR within 1 projected Mpc. Thus, the enhanced central star formation seen above is occurring in all galaxies, including the very massive ones. This is in sharp contrast to the situation at low redshift, where massive central galaxies are largely quiescent.

The sSFR distribution is higher for lower mass galaxies, as seen in the previous sections. The cluster-to-cluster variation in the SFR and sSFR, in both mass bins, is a factor of $\sim 3\text{--}5$. About half of this variation is due to the global evolution in the sSFR over the redshift range probed (Figure 7). For reference, the field galaxy sSFR values in the same mass and redshift bins, from Santini et al. (2009), are indicated with arrows.

6. DISCUSSION

6.1. The Era of Star Formation in Galaxy Clusters

These measurements of the star formation properties in high-redshift ISCS galaxy clusters expand on previous studies in several important ways. The sample of 16 IR-selected, spectroscopically confirmed $1 < z < 1.5$ clusters is the largest to date. The SFRs are measured using mid-IR photometry that is sensitive to the obscured star formation that dominates the SFR budget, and contaminating AGNs have been removed using

X-ray and mid-IR methods. The cluster sample spans the redshift interval between the era at $z \lesssim 1$, where clusters cores are less active, and the era at $z \sim 1.5$, where this trend appears to reverse. Secure spectroscopic or accurate photometric redshifts for all members, coupled with multiwavelength SED-fitted stellar masses and $24\text{ }\mu\text{m}$ based SFRs, allow robust measurement of the evolution of the SFR and sSFR in high-redshift clusters in bins of redshift, radius, and galaxy mass.

We confirm the high fraction of star-forming members in $z \gtrsim 1.4$ clusters reported by previous groups in individual clusters (e.g., Tran et al. 2010; Hilton et al. 2010; Lemaux et al. 2010; Hayashi et al. 2011; Fassbender et al. 2011a; Tadaki et al. 2012). We quantify the star-forming fraction, SFR, and sSFR, and robustly detect a transition between passive, star formation-quenched low-redshift clusters, and relatively unquenched high-redshift clusters with high central SFRs. For clusters in the mass range of the ISCS sample ($\sim 10^{14} M_\odot$ at $z > 1$), the transition to the unquenched star formation era occurs at $z \sim 1.4$.

6.2. Quenching Mechanisms

The commonly invoked quenching mechanisms in clusters, strangulation (Larson et al. 1980) and ram pressure stripping (Gunn & Gott 1972), likely operate at some level in these clusters. While the quenching timescale for strangulation (\sim several Gyr) is too long to cause the transition observed in this work, the stripping of the loosely bound outer-halo hot gas reservoirs prevents subsequent fueling and star formation episodes at late times (i.e., at $z < 1$).

Ram pressure stripping can remove tightly bound disk gas on relatively rapid timescales (~ 1 Gyr), particularly in $z > 1$ clusters in which the dynamical time is fairly short. As such, it can rapidly quench star formation in cluster galaxies. However, the ram pressure goes as the square of the orbital velocity and hence is more effective in massive, high-dispersion ($\gtrsim 1000\text{ km s}^{-1}$) clusters than in typical $z > 1$ ISCS clusters, which have more modest dispersions ($\sim 700\text{ km s}^{-1}$; Brodwin et al. 2011). Furthermore, detailed simulations of ram pressure stripping suggest that at least 30% of a galaxy's disk gas remains unstripped 10 Gyr after initial infall (McCarthy et al. 2008). Therefore, while this mechanism may be responsible for a portion of the quenching, it likely cannot fully explain the strong quenching occurring over $z = 1.5 \rightarrow 1.0$ (Figures 6 and 7). In the more passive era following the one studied in the present work, over $z \sim 1.0 \rightarrow 0.3$, Alberts et al. (2013) observe a gradual, continuous quenching of star formation in ISCS clusters. They suggest this is likely a due to a combination of strangulation and ram pressure stripping.

The transition at $z \sim 1.4$ is strikingly similar to the recent results of Mancone et al. (2010, see their Figure 7). That work measured rest-frame IR luminosity functions for the full ISCS cluster sample, consisting of 335 clusters over $0.3 < z < 2$. Using the same accurate photometric redshifts as in the present work, Mancone et al. (2010) mapped out the evolution in the cluster luminosity function at both $3.6\text{ }\mu\text{m}$ and $4.5\text{ }\mu\text{m}$. At $z < 1.3$ the evolution in the characteristic magnitude M^* , an extremely good proxy for stellar mass given the rest-frame NIR sampling, was fully consistent with the passive evolution model found in most other studies (e.g., Stanford et al. 1998). However, at $z \gtrsim 1.4$, Mancone et al. (2010) found an abrupt ~ 1 mag dimming of M^* in the cluster luminosity functions, corresponding to a stellar mass growth of a factor of ~ 2 – 4 .

from $z \sim 2$ to $z \sim 1.3$. This was interpreted as evidence of mass assembly via merging in these high-redshift cluster galaxies.

Evidence that mergers may play an important role in the evolution of galaxy populations in distant clusters has been accumulating. Luminosity functions presented by several groups exhibit a paucity of massive ($>L^*$) member galaxies on the red sequence at $z \gtrsim 1.4$ (Hilton et al. 2009, 2010; Fassbender et al. 2011a; Rudnick et al. 2012; Mancone et al. 2012). Direct and indirect evidence for a sharply increased merging rate, a factor of 3–10 higher than in contemporaneous field galaxies, has been seen in a $z = 1.62$ cluster (Lotz et al. 2013; Rudnick et al. 2012). Evidence for a stochastic star formation history, with young early-type galaxies (presumably formed via mergers) continuously arriving on the cluster red sequence at $1 < z < 1.5$, has been reported by Snyder et al. 2012 (see also Jaffé et al. 2011). A rapid two-order-of-magnitude increase in the fraction of AGN in clusters at $z \sim 1.5$ is reported by Martini et al. (2013). Finally, a high fraction of post-starburst central galaxies are detected in somewhat lower redshift ($0.6 \lesssim z \lesssim 1$) clusters (Poggianti et al. 2009; Muzzin et al. 2012).

From the *Spitzer*/IRAC data at $3.6\text{ }\mu\text{m}$ and $4.5\text{ }\mu\text{m}$, Mancone et al. (2010) could not discern whether this epoch of assembly in ISCS clusters consisted of mergers that were “wet” (i.e., collisional mergers of gas-rich galaxies, triggering a starburst and fueling black hole accretion via nuclear inflow of gas; e.g., Barnes & Hernquist 1991; Springel et al. 2005; Hopkins et al. 2006; Narayanan et al. 2010) or “dry” (collisionless mergers of gas-free galaxies; e.g., van Dokkum 2005; Bell et al. 2006). With the longer wavelength MIPS data, we now have at least circumstantial evidence that a substantial fraction of the mergers inferred by that work are likely inducing massive starbursts. Visual inspection of several of the highest L_{IR} galaxies in high-resolution *HST* images shows a large number of disturbed and/or merging systems. This evidence for “wet” mergers corroborates the findings of Desai et al. (2011) that low-redshift elliptical galaxies have residual $24\text{ }\mu\text{m}$ emission, suggestive of past collisional mergers. A complete statistical description of the star formation properties of a morphological, merger-selected sample of ISCS cluster members will be presented in a future paper.

If these observed starbursts are merger-induced, recent simulations (e.g., Springel et al. 2005; Hopkins et al. 2006; Narayanan et al. 2010) predict that AGN feedback may also play a significant role in quenching the star formation in these cluster galaxies. In these models, a merger of gas-rich progenitors both triggers massive starbursts and fuels a powerful central AGN. The AGN heats and expels the remaining gas, leading to a rapid quenching of star formation, on ~ 100 Myr timescales. This model helps explain the transition observed in the ISCS cluster galaxies and provides a mechanism that allows them to appear to be passively evolving only ~ 1 Gyr later. The most massive merger-induced starbursts will likely also experience significant feedback from supernovae and strong stellar winds, which can efficiently expel gas, particularly in the outer regions of the galaxies (Diamond-Stanic et al. 2012).

The observed starbursts are not likely to be driven by cold-mode accretion (e.g., Kereš et al. 2005; Dekel & Birnboim 2006; Dekel et al. 2009; Nelson et al. 2013) as these cluster galaxies reside within a hot ICM that should prevent cold streams to all galaxies except possibly the BCG. Furthermore, this scenario offers no straightforward way to rapidly quench the star formation for sub- L^* galaxies. The cold stream only shuts off

when the halo reaches a mass large enough ($M_{\text{halo}} \gtrsim 10^{12} M_{\odot}$) to shock heat the infalling gas. Indeed, the simulations of Kereš et al. (2005) show that cold flows are only important in areas of low galaxy density. In groups or clusters, the contribution of cold-mode accretion is expected to be negligible.

6.3. A Model for Galaxy Cluster Evolution

The standard cluster formation paradigm explains many of the observed properties of cluster galaxies. It holds that both the primordial cluster seed galaxies and those accreted from the field are stripped of their hot, loosely bound gaseous halos by the ICM. Over a dynamical time ($\lesssim 1$ Gyr in high-redshift clusters), ram pressure stripping removes of order half of the cool gas from the galaxy disks (McCarthy et al. 2008). Cold-mode accretion is inefficient in hot cluster halos (Kereš et al. 2005), so in the absence of mergers, secular star formation ceases when the remaining cool gas supply in the galaxy disks is exhausted. At this point the galaxies become quiescent and evolve passively thereafter, becoming “red and dead” by the present day. While many elements of this model are probably correct, it does not explain the extensive star formation (this work; Snyder et al. 2012; Zeimann et al. 2013; Alberts et al. 2013), merger (Mancone et al. 2010), and AGN activity (Galametz et al. 2010; Wagg et al. 2012; Martini et al. 2013) observed to be taking place in the ISCS clusters at $1 < z < 1.5$.

We find evidence for an additional, significant epoch of merging activity taking place in clusters at $z \gtrsim 1.4$, which is also the era of peak star formation and AGN activity in the general galaxy population. This merging epoch, observed statistically by Mancone et al. (2010) in the rest-frame NIR cluster luminosity functions, is occurring between gas-rich progenitors and leads to vigorous starbursts that we detect in the mid-IR. The resulting SFRs in some galaxies are so high they would, if allowed to proceed unquenched, consume the bulk of the cold gas remaining in these cluster galaxies on a very short timescale (~ 100 –300 Myr). The mergers also feed the accretion of central black holes. When these black holes enter an active AGN phase, they heat and/or expel the remaining cold gas, abruptly quenching the star formation.

This model explains the bulk of the observations of cluster evolution to date. In particular, it offers a more physically motivated explanation for the apparent pure passive evolution seen in $z < 1$ cluster studies (e.g., Stanford et al. 1998; van Dokkum & van der Marel 2007; Muzzin et al. 2008). These studies typically employ models in which the last significant star formation activity occurred at $z > 2$. These models are ruled out by recent observations of vigorous star formation in high-redshift clusters, most dramatically in the present paper. While a passive model fit the Mancone et al. (2010) observations for clusters at $z \lesssim 1.3$, it failed completely at higher redshift, where the galaxies were substantially less massive than expected in a merger-free passive model. Similarly, the rapid reddening observed in E08 at $z \sim 1.4$ (their Figure 19) is better explained by an epoch of merger-driven obscured star formation than by a sudden change in the passive-model formation redshift from $z_f \sim 4$ to $z_f \sim 30$. In the AGN-quenched model, cluster galaxies will have faded, reddened, and appear “red and dead” by $z \sim 1$ (1–2 Gyr after quenching). If the galaxies evolve passively thereafter, they will appear in the present day to have luminosity-weighted pure passive-model formation redshifts of $2 \lesssim z \lesssim 4$. That is an average of the more extended and punctuated star formation history, from formation at $z \gtrsim 4$ to final starburst ending at $z \sim 1.4$.

Indeed, recent analyses of the colors and scatters of red sequences in high-redshift clusters, such as Jaffé et al. (2011) and Snyder et al. (2012), have tested models with ongoing stochastic or even continuous star formation, ending 1–2 Gyr prior to the epoch of observation. They find good fits for models in which the interval between formation and final placement on the cluster red sequence is similar to the timescale for AGN-quenching in mergers. These delayed models, in which the last big epoch of star formation occurs at $z < 2$ but is complete by $z \sim 1.2$, are qualitatively consistent with the ISCS cluster observations and the picture we have presented to describe them.

Unlike explanations of low-redshift galaxy properties, such as the black hole–bulge mass relation (e.g., Ferrarese & Merritt 2000) or the very red colors of the most massive field galaxies (e.g., Croton et al. 2006), mergers in this work were not merely invoked as a useful mechanism to explain the observations. The era of significant merging was first *observed* (statistically) in Mancone et al. (2010), and in the present work we directly observe in the same clusters the vigorous starbursts expected from gas-rich mergers. Furthermore, we indirectly observe the expected rapid quenching of the star formation due to feedback from the central AGN. The AGN feedback scenario offers a natural explanation for all these observations and, furthermore, makes several falsifiable predictions.

It most directly predicts a strong increase in the incidence of AGN activity in clusters at $z > 1$ compared with those at lower redshifts. Evidence of this has already been seen by several groups (e.g., Martini et al. 2009; Kocevski et al. 2009a; Lemaux et al. 2010; Tanaka et al. 2013; Fassbender et al. 2012), including our own statistical analysis of the full ISCS sample (Galametz et al. 2009) in which we find that X-ray-selected AGNs are at least three times more prevalent in clusters at $1 < z < 1.5$ compared with clusters at $0.5 < z < 1$. Since cold flows are inefficient in hot cluster halos, the role of mergers in rich environments is likely to be even more important than in the field. Therefore, we might expect not only a rapid increase in the incidence of AGN activity in clusters with increasing redshift but also an increase that is significantly *more* rapid than is occurring in the field. A detailed new analysis of the clusters in this work (Martini et al. 2013), using deep X-ray data and extensive spectroscopy, confirms this is the case. Although the AGN fraction is ≈ 6 times higher in the field than in clusters in the local Universe, the fractions are comparable at $z \sim 1.25$. Martini et al. (2013) conclude that this differential evolution of the AGN fraction in the field and clusters is strong evidence for environment-dependent AGN evolution.

This model also corroborates the findings of Brodwin et al. (2008) that the brightest dust-obscured galaxies (DOGs; Dey et al. 2008; Pope et al. 2008), which are dusty AGN-dominated ULIRGs at $1.5 \lesssim z \lesssim 2.5$ (also see Farrah et al. 2006; Magliocchetti et al. 2008; Viero et al. 2013; Starikova et al. 2012), have similar clustering properties to galaxy groups and are located in rare, rich environments. Although this extreme population is excluded from the present study by our AGN rejection and the limited redshift overlap with the clusters in this sample, this evolutionary relationship between DOGs and clusters is an interesting and important topic that will be addressed in a future paper (Williams et al., in preparation).

In addition to rendering cluster galaxies largely quiescent at $z \lesssim 1$, in this model cluster galaxies at such redshifts should show signs of both recent starburst activity and of rapid AGN-driven quenching. This is seen in a several studies, with high post-starburst and low-level AGN fractions in clusters at

$0.8 \lesssim z \lesssim 1$ (e.g., Kocevski et al. 2009b; Lemaux et al. 2010; Muzzin et al. 2012).

6.4. Epoch of Merging in ISCS Clusters

Mergers are most efficient when galaxy space densities are high and relative velocities are low. In the local Universe, group environments, with their relatively high source densities and modest velocity dispersions, are expected to have the highest merging frequency (Hopkins et al. 2008). Dispersion are too high ($>1000 \text{ km s}^{-1}$) in present-day massive clusters ($M \sim 10^{15} M_{\odot}$) to produce much merging. But the $z > 1$ progenitors of these massive clusters had smaller halo masses and velocity dispersions, and higher densities of galaxies with extended gas-rich disks, all of which led to a higher merging efficiency. For clusters with masses typical of the ISCS sample ($\sim 10^{14} M_{\odot}$ at $z > 1$), major merging had likely been occurring continuously since initial formation but should have begun to subside by $z \sim 1.5$ because of ever-growing velocity dispersions. Indeed, in their long-baseline *Herschel* stacking study, Alberts et al. (2013) only find evidence for substantial merging in ISCS clusters at $z \gtrsim 1.4$. An enhanced merger rate is also directly observed in CIG J0218.3–0510 at $z = 1.62$ (Lotz et al. 2013) and inferred by Rudnick et al. (2012) from the evolution of its luminosity function.

If this model is correct, more massive high-redshift clusters such as SPT-CL J0205–5829 at $z = 1.32$ (Stalder et al. 2013), XMMU J2235.3–2557 at $z = 1.39$ (Mullis et al. 2005; Rosati et al. 2009), and SPT-CL J2040–4451 at $z = 1.48$ (Bayliss et al. 2013), with masses of $\sim 9 \times 10^{14} M_{\odot}$, $\sim 6 \times 10^{14} M_{\odot}$, and $\sim 6 \times 10^{14} M_{\odot}$, respectively, should no longer be experiencing efficient merging because of their high in situ velocity dispersions. Rather, their transition redshifts, when phase space conditions were more conducive to major merging activity, should be considerably higher than that seen in the ISCS. Indeed, these clusters have relatively low central SFRs (Stalder et al. 2013; Grützbauch et al. 2012; Bayliss et al. 2013; Santos et al. 2013) that are $\lesssim 5 \times$ below those in the present work, consistent with already being largely quenched and passive in their cores. A related prediction is that the scatter in the colors of red-sequence galaxies in these very massive clusters should be smaller than that measured by Snyder et al. (2012) for ISCS clusters at similar redshifts.

Another test of this prediction, using the massive cluster IDCS J1426.5+3508 at $z = 1.75$ (Brodwin et al. 2012; Gonzalez et al. 2012; Stanford et al. 2012), is forthcoming. This cluster is, in an evolutionary sense, a precursor of these three massive clusters and of the most massive clusters at all redshifts, including Coma. Its star formation properties, measured from deep *Herschel* observations, will be presented in an upcoming paper (S. Alberts et al., in preparation). Though very massive for its redshift ($M_{200} \sim 4 \times 10^{14} M_{\odot}$), it is very compact, with the majority of the IR overdensity within a projected radius of $\sim 30''$. As such, conditions may be still be suitable for substantial merging and merging-induced starbursts.

7. CONCLUSIONS

We have investigated the star formation properties of 16 high-redshift, IR-selected galaxy clusters from the ISCS. Using deep *Spitzer* 24 μm imaging, we characterized the obscured star formation in these clusters as a function of redshift, stellar mass, and clustercentric radius. For six of these clusters, including five at $z > 1.35$, we also provide the ground-based spectroscopic

confirmation. Redshifts from the *HST*/WFC3 grism, along with a complementary analysis of the unobscured H α star formation activity, are presented in Zeimann et al. (2013).

The primary result is that $z > 1$ ISCS clusters have substantial star formation activity occurring at all radii, including in the cluster cores. The SFRs in these cluster galaxies are similar to that of field galaxies at similar redshifts, suggesting that we are probing the era before cluster quenching was complete. As we have conservatively rejected X-ray and IR AGNs from this study, these cluster SFRs are lower limits.

The transition between the low redshift ($z < 1$) era, in which cluster galaxies are significantly quenched relative to the field, and the era of cluster formation, in which cluster galaxies form stars at the same rate as field galaxies for their masses, occurs at $z \sim 1.4$ in the ISCS sample. Below this redshift, although significant star formation occurs in clusters at all radii, the sSFR drops near the core, suggesting active environment-dependent quenching. At redshifts above $z \sim 1.4$, there is evidence from both the fraction of star-forming galaxies and the sSFR that quenching in the cores is minimal. Above this redshift, cluster galaxies are forming stars at the rate expected for field galaxies of similar mass, independent of their location in the cluster.

There is a factor of $\sim 3\text{--}5$ variation in the star formation activity from cluster to cluster in this IR-selected sample. About half of that variation is due to the observed redshift evolution, but the rest is intrinsic scatter in the population. This variance suggests that substantially larger samples will be required to improve upon the present work. In particular, single-cluster studies are difficult to interpret and to place in a meaningful evolutionary context.

Combining the present measurements with recent independent results from the ISCS survey, such as the strong increase in AGN density (Martini et al. 2013), the stochastic star formation histories (Snyder et al. 2012; Alberts et al. 2013), and the statistical evidence for a significant assembly epoch at ~ 1.4 (Mancone et al. 2010), we suggest that mergers likely play a significant role in the observed star formation activity. In addition to plausibly inducing the large starbursts seen in these cluster galaxies, merger-fueled AGN feedback (e.g., Hopkins et al. 2006) may naturally explain the rapid truncation of star formation that occurs between $z \sim 1.5$ and $z \lesssim 1$, by which time the cores of clusters become largely quiescent (e.g., Vulcani et al. 2010; Finn et al. 2010; Muzzin et al. 2012) with high post-starburst fractions (Poggianti et al. 2009; Muzzin et al. 2012).

If mergers do play a significant role in the transition between the unquenched and quenched eras, the redshift of this transition is likely strongly dependent on cluster halo mass. Mergers require relatively low velocity dispersions, so a prediction of this work is that more massive clusters than those in the ISCS sample would experience this transition at higher redshifts. Studies of the star formation properties in the few known high-mass, high-redshift clusters (Stalder et al. 2013; Grützbauch et al. 2012; Bayliss et al. 2013; Santos et al. 2013) support this expectation.

This work is based in part on observations made with the *Spitzer Space Telescope*, which is operated by the Jet Propulsion Laboratory, California Institute of Technology under a contract with NASA. Support for this work was provided by NASA through an award issued by JPL/Caltech. Support for HST programs 10496, 11002, 11597, and 11663 were provided by NASA through a grant from the Space Telescope Science Institute, which is operated by the Association of Universities for Research in Astronomy, Inc., under NASA contract

NAS 5-26555. This work is based in part on observations obtained with the *Chandra X-ray Observatory*, under contract SV4-74018, A31 with the Smithsonian Astrophysical Observatory which operates the *Chandra X-ray Observatory* for NASA. Support for this research was provided by NASA grant G09-0150A. This work is based in part on data obtained at the W. M. Keck Observatory, which is operated as a scientific partnership among the California Institute of Technology, the University of California, and the National Aeronautics and Space Administration. The Observatory was made possible by the generous financial support of the W. M. Keck Foundation. This work makes use of image data from the NOAO Deep Wide-Field Survey (NDWFS) as distributed by the NOAO Science Archive. NOAO is operated by the Association of Universities for Research in Astronomy (AURA), Inc., under a cooperative agreement with the National Science Foundation.

We are grateful to the referee for a helpful report that improved the clarity of the paper. We thank P. Santini for providing her data in a digital form. We appreciate several useful conversations with C. Papovich, M. Cooper, M. Dickinson, N. Reddy, and S. Salim. This paper would not have been possible without the efforts of the support staffs of the *Spitzer Space Telescope*, *Hubble Space Telescope*, *Chandra X-ray Observatory*, and W. M. Keck Observatory.

REFERENCES

- Alberts, S., Pope, A., Brodwin, M., et al. 2013, *MNRAS*, in press (arXiv:1310.6040)
- Ashby, M. L. N., Stern, D., Brodwin, M., et al. 2009, *ApJ*, **701**, 428
- Bai, L., Marcillac, D., Rieke, G. H., et al. 2007, *ApJ*, **664**, 181
- Bai, L., Rieke, G. H., Rieke, M. J., Christlein, D., & Zabludoff, A. I. 2009, *ApJ*, **693**, 1840
- Barnes, J. E., & Hernquist, L. E. 1991, *ApJL*, **370**, L65
- Bayliss, M. B., Ashby, M. L. N., Ruel, J., et al. 2013, *ApJ*, submitted (arXiv:1307.2903)
- Bell, E. F., McIntosh, D. H., Katz, N., & Weinberg, M. D. 2003, *ApJS*, **149**, 289
- Bell, E. F., Naab, T., McIntosh, D. H., et al. 2006, *ApJ*, **640**, 241
- Blakeslee, J. P., Holden, B. P., Franx, M., et al. 2006, *ApJ*, **644**, 30
- Brodwin, M., Brown, M. J. I., Ashby, M. L. N., et al. 2006, *ApJ*, **651**, 791
- Brodwin, M., Dey, A., Brown, M. J. I., et al. 2008, *ApJL*, **687**, L65
- Brodwin, M., Gonzalez, A. H., Moustakas, L. A., et al. 2007, *ApJL*, **671**, L93
- Brodwin, M., Gonzalez, A. H., Stanford, S. A., et al. 2012, *ApJ*, **753**, 162
- Brodwin, M., Stern, D., Vikhlinin, A., et al. 2011, *ApJ*, **732**, 33
- Bruzual, G., & Charlot, S. 2003, *MNRAS*, **344**, 1000
- Chabrier, G. 2003, *PASP*, **115**, 763
- Chary, R., & Elbaz, D. 2001, *ApJ*, **556**, 562
- Chung, S. M., Eisenhardt, P. R., Gonzalez, A. H., et al. 2011, *ApJ*, **743**, 34
- Chung, S. M., Gonzalez, A. H., Clowe, D., Markevitch, M., & Zaritsky, D. 2010, *ApJ*, **725**, 1536
- Coia, D., McBreen, B., Metcalfe, L., et al. 2005, *A&A*, **431**, 433
- Coleman, G. D., Wu, C.-C., & Weedman, D. W. 1980, *ApJS*, **43**, 393
- Cooper, M. C., Newman, J. A., Weiner, B. J., et al. 2008, *MNRAS*, **383**, 1058
- Croton, D. J., Springel, V., White, S. D. M., et al. 2006, *MNRAS*, **365**, 11
- Dekel, A., & Birnboim, Y. 2006, *MNRAS*, **368**, 2
- Dekel, A., Birnboim, Y., Engel, G., et al. 2009, *Natur*, **457**, 451
- Desai, V., Dey, A., Cohen, E., Le Floc'h, E., & Soifer, B. T. 2011, *ApJ*, **730**, 130
- Dey, A., Soifer, B. T., Desai, V., et al. 2008, *ApJ*, **677**, 943
- Diamond-Stanic, A. M., Moustakas, J., Tremonti, C. A., et al. 2012, *ApJL*, **755**, L26
- Eisenhardt, P. R., Stern, D., Brodwin, M., et al. 2004, *ApJS*, **154**, 48
- Eisenhardt, P. R. M., Brodwin, M., Gonzalez, A. H., et al. 2008, *ApJ*, **684**, 905
- Elbaz, D., Daddi, E., Le Borgne, D., et al. 2007, *A&A*, **468**, 33
- Elbaz, D., Hwang, H. S., Magnelli, B., et al. 2010, *A&A*, **518**, L29
- Elston, R. J., Gonzalez, A. H., McKenzie, E., et al. 2006, *ApJ*, **639**, 816
- Farrah, D., Lonsdale, C. J., Borys, C., et al. 2006, *ApJL*, **643**, L139
- Fassbender, R., Bhringer, H., Nastasi, A., et al. 2011a, *NJPh*, **13**, 125014
- Fassbender, R., Nastasi, A., Bhringer, H., et al. 2011b, *A&A*, **527**, L10
- Fassbender, R., Šuhada, R., & Nastasi, A. 2012, *AdAst*, **2012**, 138380
- Ferrarese, L., & Merritt, D. 2000, *ApJL*, **539**, L9
- Finn, R. A., Desai, V., Rudnick, G., et al. 2010, *ApJ*, **720**, 87
- Galametz, A., Stern, D., Eisenhardt, P. R. M., et al. 2009, *ApJ*, **694**, 1309
- Galametz, A., Stern, D., Stanford, S. A., et al. 2010, *A&A*, **516**, A101
- Geach, J. E., Smail, I., Ellis, R. S., et al. 2006, *ApJ*, **649**, 661
- Gonzalez, A. H., Stanford, S. A., Brodwin, M., et al. 2012, *ApJ*, **753**, 163
- Grützbauch, R., Bauer, A. E., Jørgensen, I., & Varela, J. 2012, *MNRAS*, **423**, 3652
- Gunn, J. E., & Gott, J. R., III. 1972, *ApJ*, **176**, 1
- Haines, C. P., Smith, G. P., Egami, E., et al. 2009, *ApJ*, **704**, 126
- Hayashi, M., Kodama, T., Koyama, Y., Tadaki, K.-I., & Tanaka, I. 2011, *MNRAS*, **415**, 2670
- Hilton, M., Lloyd-Davies, E., Stanford, S. A., et al. 2010, *ApJ*, **718**, 133
- Hilton, M., Stanford, S. A., Stott, J. P., et al. 2009, *ApJ*, **697**, 436
- Hopkins, P. F., Hernquist, L., Cox, T. J., & Kereš, D. 2008, *ApJS*, **175**, 356
- Hopkins, P. F., Hernquist, L., Cox, T. J., et al. 2006, *ApJS*, **163**, 1
- Jaffé, Y. L., Aragón-Salamanca, A., De Lucia, G., et al. 2011, *MNRAS*, **410**, 280
- Jannuzzi, B. T., & Dey, A. 1999, in ASP Conf. Ser. 191, Photometric Redshifts and the Detection of High Redshift Galaxies, ed. R. Weymann, L. Storrie-Lombardi, M. Sawicki, & R. Brunner (San Francisco, CA: ASP), **111**
- Jee, M. J., Dawson, K. S., Hoekstra, H., et al. 2011, *ApJ*, **737**, 59
- Kereš, D., Katz, N., Weinberg, D. H., & Davé, R. 2005, *MNRAS*, **363**, 2
- Kinney, A. L., Calzetti, D., Bohlin, R. C., et al. 1996, *ApJ*, **467**, 38
- Kocevski, D. D., Lubin, L. M., Gal, R., et al. 2009a, *ApJ*, **690**, 295
- Kocevski, D. D., Lubin, L. M., Lemaux, B. C., et al. 2009b, *ApJ*, **700**, 901
- Kochanek, C. S., Eisenstein, D. J., Cool, R. J., et al. 2012, *ApJS*, **200**, 8
- Komatsu, E., Smith, K. M., Dunkley, J., et al. 2011, *ApJS*, **192**, 18
- Koyama, Y., Kodama, T., Shimakawa, K., et al. 2008, *MNRAS*, **391**, 1758
- Krick, J. E., Surace, J. A., Thompson, D., et al. 2009, *ApJ*, **700**, 123
- Kroupa, P. 2001, *MNRAS*, **322**, 231
- Larson, R. B., Tinsley, B. M., & Caldwell, C. N. 1980, *ApJ*, **237**, 692
- Le Borgne, J.-F., Bruzual, G., Pell, R., et al. 2003, *A&A*, **402**, 433
- Lemaux, B. C., Lubin, L. M., Shapley, A., et al. 2010, *ApJ*, **716**, 970
- Lotz, J. M., Papovich, C., Faber, S. M., et al. 2013, *ApJ*, **773**, 154
- Magliocchetti, M., Cirasuolo, M., McLure, R. J., et al. 2008, *MNRAS*, **383**, 1131
- Magnelli, B., Elbaz, D., Chary, R. R., et al. 2009, *A&A*, **496**, 57
- Mancone, C. L., Baker, T., Gonzalez, A. H., et al. 2012, *ApJ*, **761**, 141
- Mancone, C. L., Gonzalez, A. H., Brodwin, M., et al. 2010, *ApJ*, **720**, 284
- Marcillac, D., Elbaz, D., Chary, R. R., et al. 2006, *A&A*, **451**, 57
- Marcillac, D., Rigby, J. R., Rieke, G. H., & Kelly, D. M. 2007, *ApJ*, **654**, 825
- Martini, P., Miller, E. D., Brodwin, M., et al. 2013, *ApJ*, **768**, 1
- Martini, P., Sivakoff, G. R., & Mulchaey, J. S. 2009, *ApJ*, **701**, 66
- McCarthy, I. G., Frenk, C. S., Font, A. S., et al. 2008, *MNRAS*, **383**, 593
- Mei, S., Holden, B. P., Blakeslee, J. P., et al. 2009, *ApJ*, **690**, 42
- Moustakas, J., Coil, A. L., Aird, J., et al. 2013, *ApJ*, **767**, 50
- Mullis, C. R., Rosati, P., Lamer, G., et al. 2005, *ApJL*, **623**, L85
- Murphy, E. J., Chary, R., Alexander, D. M., et al. 2009, *ApJ*, **698**, 1380
- Murphy, E. J., Condon, J. J., Schinnerer, E., et al. 2011, *ApJ*, **737**, 67
- Murray, S. S., Kenter, A., Forman, W. R., et al. 2005, *ApJS*, **161**, 1
- Muzzin, A., Wilson, G., Lacy, M., Yee, H. K. C., & Stanford, S. A. 2008, *ApJ*, **686**, 966
- Muzzin, A., Wilson, G., Yee, H. K. C., et al. 2012, *ApJ*, **746**, 188
- Narayanan, D., Dey, A., Hayward, C. C., et al. 2010, *MNRAS*, **407**, 1701
- Nelson, D., Vogelsberger, M., Genel, S., et al. 2013, *MNRAS*, **429**, 3353
- Nordon, R., Lutz, D., Shao, L., et al. 2010, *A&A*, **518**, L24
- Poggianti, B. M., Aragón-Salamanca, A., Zaritsky, D., et al. 2009, *ApJ*, **693**, 112
- Polletta, M., Tajer, M., Maraschi, L., et al. 2007, *ApJ*, **663**, 81
- Pope, A., Chary, R.-R., Alexander, D. M., et al. 2008, *ApJ*, **675**, 1171
- Rodighiero, G., Cimatti, A., Gruppioni, C., et al. 2010, *A&A*, **518**, L25
- Rosati, P., Tozzi, P., Gobat, R., et al. 2009, *A&A*, **508**, 583
- Rudnick, G. H., Tran, K.-V., Papovich, C., Momcheva, I., & Willmer, C. 2012, *ApJ*, **755**, 14
- Saintonge, A., Tran, K., & Holden, B. P. 2008, *ApJL*, **685**, L113
- Santini, P., Fontana, A., Grazian, A., et al. 2009, *A&A*, **504**, 751
- Santos, J. S., Altieri, B., Popesso, P., et al. 2013, *MNRAS*, **433**, 1287
- Santos, J. S., Fassbender, R., Nastasi, A., et al. 2011, *A&A*, **531**, L15
- Smith, G. P., Haines, C. P., Pereira, M. J., et al. 2010, *A&A*, **518**, L18
- Snyder, G. F., Brodwin, M., Mancone, C. M., et al. 2012, *ApJ*, **756**, 114
- Springel, V., White, S. D. M., Jenkins, A., et al. 2005, *Natur*, **435**, 629
- Stalder, B., Ruel, J., Šuhada, R., et al. 2013, *ApJ*, **763**, 93
- Stanford, S. A., Brodwin, M., Gonzalez, A. H., et al. 2012, *ApJ*, **753**, 164
- Stanford, S. A., Eisenhardt, P. R., Brodwin, M., et al. 2005, *ApJL*, **634**, L129
- Stanford, S. A., Eisenhardt, P. R., & Dickinson, M. 1998, *ApJ*, **492**, 461
- Starikova, S., Berta, S., Franceschini, A., et al. 2012, *ApJ*, **751**, 126
- Stern, D., Eisenhardt, P., Gorjian, V., et al. 2005, *ApJ*, **631**, 163
- Stetson, P. B. 1987, *PASP*, **99**, 191
- Tadaki, K.-i., Kodama, T., Ota, K., et al. 2012, *MNRAS*, **423**, 3652

- Tanaka, M., Finoguenov, A., Mirkazemi, M., et al. 2013, PASJ, **65**, 17
Tran, K., Papovich, C., Saintonge, A., et al. 2010, ApJL, **719**, L126
Tran, K.-V. H., Saintonge, A., Moustakas, J., et al. 2009, ApJ, **705**, 809
van Dokkum, P. G. 2005, AJ, **130**, 2647
van Dokkum, P. G., & van der Marel, R. P. 2007, ApJ, **655**, 30
Viero, M. P., Wang, L., Zemcov, M., et al. 2013, ApJ, **772**, 77
- Vulcani, B., Poggianti, B. M., Finn, R. A., et al. 2010, ApJL, **710**, L1
Wagg, J., Pope, A., Alberts, S., et al. 2012, ApJ, **752**, 91
Webb, T., O'Donnell, D., Yee, H. K. C., et al. 2013, AJ, **146**, 84
White, S. D. M., Clowe, D. I., Simard, L., et al. 2005, A&A, **444**, 365
Zeimann, G. R., Stanford, S. A., Brodwin, M., et al. 2012, ApJ, **756**, 115
Zeimann, G. R., Stanford, S. A., Brodwin, M., et al. 2013, ApJ, 779, 137